



## Nanostructured, Glassy-Carbon-Supported Pt/GC Electrodes: The Presence of Secondary Pt Nanostructures and How to Avoid Them

Y. E. Seidel,<sup>a</sup> M. Müller,<sup>a</sup> Z. Jusys,<sup>a</sup> B. Wickman,<sup>b</sup> P. Hanarp,<sup>b</sup> B. Kasemo,<sup>b</sup>  
U. Hörmann,<sup>c</sup> U. Kaiser,<sup>c</sup> and R. J. Behm<sup>a,\*</sup>

<sup>a</sup>Institute of Surface Chemistry and Catalysis and <sup>c</sup>Central Facility for Electron Microscopy, Ulm University, D-89069 Ulm, Germany

<sup>b</sup>Department of Applied Physics, Chalmers University of Technology, S-41296 Göteborg, Sweden

Nanostructured, glassy carbon (GC) supported Pt/GC electrodes, with Pt nanostructures (nanodisks) of controlled size (100–140 nm in diameter) and separation homogeneously distributed on a planar GC substrate, were recently shown to be interesting model systems for electrocatalytic reaction studies [M. Gustavsson, H. Fredriksson, B. Kasemo, Z. Jusys, C. Jun, and R. J. Behm, *J. Electroanal. Chem.*, **568**, 371 (2004)]. We present here electron microscopy and electrochemical measurements which reveal that the fabrication of these nanostructured electrodes via colloidal lithography, in addition to the intended nanodisks, results in a dilute layer of much smaller Pt nanoparticles (diameter  $\sim 5$  nm) on the GC surface in the areas between the Pt nanodisks. We further demonstrate that by using the developed, related method of hole-mask colloidal lithography (HCL) [H. Fredriksson, Y. Alaverdyan, A. Dmitriev, C. Langhammer, D. S. Sutherland, M. Zäch, and B. Kasemo, *Adv. Mater. (Weinheim, Ger.)*, **19**, 4297 (2007)], similar electrodes can be prepared which are free from these Pt nanoparticles. The effect of the additional small Pt nanoparticles on the electrochemical and electrocatalytic properties of these nanostructured electrodes, which is significant and can become dominant at low densities of the Pt nanodisks, is illustrated and discussed. These results leave HCL the preferred method for the fabrication of nanostructured Pt/GC electrodes, in particular, of low-density Pt/GC electrodes.  
© 2008 The Electrochemical Society. [DOI: 10.1149/1.2956326] All rights reserved.

Manuscript submitted April 22, 2008; revised manuscript received June 18, 2008. Published July 29, 2008.

Model studies of catalytic and electrocatalytic reactions, performed on structurally and chemically well-defined, but nevertheless more realistic systems than, e.g., polycrystalline or single-crystal (electrode) surfaces and under close-to-realistic reaction conditions (e.g., pressure, temperature, particle-support interactions), have attracted increasing interest in recent years.<sup>1–4</sup> Making use of new developments in the area of surface nanostructuring,<sup>5–13</sup> we recently introduced colloidal lithography (CL) as a tool for the controlled preparation of planar nanostructured electrodes with defined particle sizes and particle distances.<sup>12,14</sup> In this way, we could prepare nanostructured electrodes consisting of a planar glassy carbon (GC) substrate with electrochemically active Pt nanostructures (nanodisks) of adjustable, similar size ( $\varnothing 80$ –140 nm) deposited on top. In addition to the narrow size distribution, the nanodisks are arranged in a rather regular array with a narrow distribution of interparticle separations, which uniformly covers the entire accessible electrode area. Both the size of the Pt nanodisks and their separation can be varied independently and in a controlled way. Hence, this method extends the possibilities of earlier lithographic approaches (compare Ref. 5–7, 15, and 16) for the preparation of such array structures, allowing the fabrication of arrays of ultramicroelectrodes with electrode sizes in the 100 nm range. Due to the well-defined arrangement of the nanodisks, which is much more regular than the statistical distribution of nanoparticles obtained, e.g., by physical vapor deposition or electrodeposition of metals, these model systems are ideally suited for studying transport and diffusion processes. Furthermore, they provide ideal test systems for simulations of these processes on arrays of microelectrodes.<sup>17–22</sup>

These nanostructured planar electrodes were used as model systems for studies of the role of transport effects in electrocatalytic reactions, investigating the effect of the nanodisk density on their electrochemical and electrocatalytic properties.<sup>23,24</sup> The influence of the preparation process on the stability of the active nanodisks during electrochemical/electrocatalytic measurements was investigated in detail and optimized to an extent that the resulting nanodisks are fully stable also during continuous electrolyte flow and continuous

reaction conditions.<sup>25</sup> In addition to these electrocatalytic model studies, CL was also applied for preparing membrane electrode assemblies for fuel cell studies.<sup>26</sup>

In order to extend the parameter range in these studies, we reduced this density of Pt nanodisks to very low values, with the Pt nanodisks ( $\varnothing 140$  nm) covering about 1% of the electrode surface (Pt surface coverage  $\sim 1\%$ ). Previous measurements on these samples had shown, however, that the electrochemical active Pt surface area determined by hydrogen underpotential deposition ( $H_{\text{upd}}$ ) and  $\text{CO}_{\text{ad}}$  monolayer oxidation (“ $\text{CO}_{\text{ad}}$  stripping”) is much higher than expected by comparison with higher coverage samples or than calculated from the density, size, and shape of the nanostructures derived from scanning electron microscopy (SEM) images.

In the present paper we try to elucidate the origin of this deviating electrochemical behavior observed for nanostructured Pt/GC electrodes with very low densities of Pt nanodisks by detailed electron microscopy studies and by comparing the electrochemical properties of the very-low-density Pt/GC electrodes with those of samples with higher densities of similar size Pt nanodisks (Pt coverage  $\sim 20$  and  $\sim 40\%$ ), which were prepared in the same way. Electron microscopy measurements include high-resolution SEM and locally resolved elemental analysis by energy-dispersive X-ray analysis (EDX), as well as conventional and high-resolution transmission electron microscopy (CTEM and HRTEM) on cross-sectional samples. Furthermore, we introduce the newly developed, related method of hole-mask colloidal lithography (HCL)<sup>13</sup> for the preparation of similar type nanostructured electrodes and characterize their structural and electrochemical properties. Measurements of the electrocatalytic properties of CL- and HCL-prepared nanostructured electrodes ( $\text{CO}$  bulk oxidation and formaldehyde oxidation) will be published elsewhere.<sup>24</sup>

After a brief description of the experimental setup and procedures and of the preparation of the nanostructured electrodes, we first characterize the morphology and surface composition of the nanostructured electrodes by high-resolution SEM, CTEM, and HRTEM on cross-sectional samples and by locally resolved elemental analysis by EDX. In the second part, we concentrate on the electrochemical characterization of the Pt/GC model systems, by cyclic voltammetry (CV) and preadsorbed  $\text{CO}$  monolayer oxidation ( $\text{CO}_{\text{ad}}$  stripping). The results are discussed with special attention on identifying and understanding the origin of the substantial difference

\* Electrochemical Society Active Member.

<sup>z</sup> E-mail: juergen.behm@uni-ulm.de

**Table I.** Geometrical data of the different nanostructured Pt/GC electrodes, as determined by SEM, assuming cylindrical Pt nanodisks and spherical Pt nanoparticles (see Table II). The Pt coverage is defined as the fraction of the GC surface covered by the projection of the Pt nanodisks and nanoparticles.

Sample	Pt	Diameter (nm)	Density ( $\mu\text{m}^2$ )	Pt surface coverage (%)	Geom. Pt surface area ( $\text{cm}^2$ )
CL-40	Nanodisks	$140 \pm 24$	26	40	0.18
	Nanoparticles	$3.9 \pm 2.6$	2510	3	0.034
	<b>Total</b>	—	—	<b>43</b>	<b>0.21</b>
CL-20	Nanodisks	$134 \pm 19$	16	22	0.10
	Nanoparticles	$4.3 \pm 3.2$	2760	4	0.045
	<b>Total</b>	—	—	<b>26</b>	<b>0.14</b>
CL-01	Nanodisks	$147 \pm 6$	0.5	0.8	0.003
	Nanoparticles	$6.5 \pm 4$	1810	6	0.068
	<b>Total</b>	—	—	<b>6.8</b>	<b>0.071</b>
CL-00	Nanoparticles	$7.3 \pm 4$	1670	7	0.079
HCL-20	Nanodisks	$118 \pm 12$	20	22	0.10
HCL-10	Nanodisks	$94 \pm 99$	14	10	0.052

between the expected and experimentally observed electrochemical behavior of the low-Pt-coverage, CL-prepared Pt/GC electrodes.

### Experimental

We investigated five different types of nanostructured Pt/GC electrodes with Pt nanodisks of 100–140 nm in diameter and different separations and, correspondingly, different Pt coverages. These include (i) high-loading samples (CL-40) with  $\sim 40\%$  Pt coverage ( $\varnothing \sim 140$  nm), (ii) medium-loading samples (CL-20) with  $\sim 22\%$  Pt coverage ( $\varnothing \sim 134$  nm), and (iii) ultralow-loading samples (CL-01) with  $\sim 1\%$  Pt coverage ( $\varnothing \sim 147$  nm), all of which were prepared by CL. Furthermore, we included (iv) medium-loading (HCL-20) and (v) low-loading (HCL-10) samples with  $\sim 22\%$  Pt and  $10\%$  Pt coverage, respectively ( $\varnothing \sim 118$  and  $\sim 94$  nm), both prepared by HCL. All experiments were performed on three different samples of each type to ensure reproducibility. As references, we (vi) also included nonstructured samples, where the initial Pt film was completely removed by  $\text{Ar}^+$  sputtering (CL-00), and a bare GC. The structural characteristics of the nanostructured electrodes used in the present study are summarized in Table I.

**Catalyst preparation and characterization.**— Well-defined arrays of Pt nanodisks on GC support were prepared by colloidal and hole-mask colloidal lithography, employing the procedure described in detail in Ref. 9, 10, 13, and 14. A schematic description of both methods is given in Fig. 1.

The GC substrates were prepared as already described in Ref. 25. In brief, GC disks ( $\varnothing \sim 9$  mm, Sigradur Hochtemperatur Werkstoffe GmbH) were polished with alumina slurry down to  $0.3 \mu\text{m}$  grid, cleaned by immersion in  $5 \text{ M KOH}$ , and rinsed in Millipore Milli-Q water (resistivity  $> 18 \text{ M}\Omega \text{ cm}$ ). They were subsequently immersed in concentrated  $\text{H}_2\text{SO}_4$  (aq), again rinsed with Millipore Milli-Q water, and finally dried in a  $\text{N}_2$  stream. The substrate surface was first treated in an oxygen plasma ( $50 \text{ W}$ ,  $330 \text{ mbar}$ ,  $2 \text{ min}$ ). For the CL samples, an in situ argon plasma ( $50 \text{ W}$ ,  $13 \text{ mbar}$ ,  $2 \text{ min}$ ) was then used before a  $20 \text{ nm}$  thick Pt film was sputter-deposited (Nordiko 2000 Sputter). For CL processing (Fig. 1A), a dilute layer of negatively charged polystyrene (PS) colloid particles ( $\varnothing 110 \text{ nm}$ ) was deposited on the pristine Pt film by pipetting (Fig. 1A, c). Due to the repulsion between the charged PS particles, a well-ordered PS-particle adlayer was formed. For the high loading CL-40 sample (high coverage of nanodisks),  $0.2 \text{ mM NaCl}$  was added to the aqueous suspension to reduce the PS particle repulsion (shorter Debye screening length) and create a denser adlayer.<sup>10</sup> The PS particles were transformed from spherical to hemispherical shape by premelting them on a hot plate ( $118^\circ\text{C}$ ,  $2 \text{ min}$ ), which in the further processing leads to flat Pt nanodisks.<sup>14,26</sup> The unprotected Pt film between the colloid particles was then removed by  $\text{Ar}^+$  sputtering ( $500$

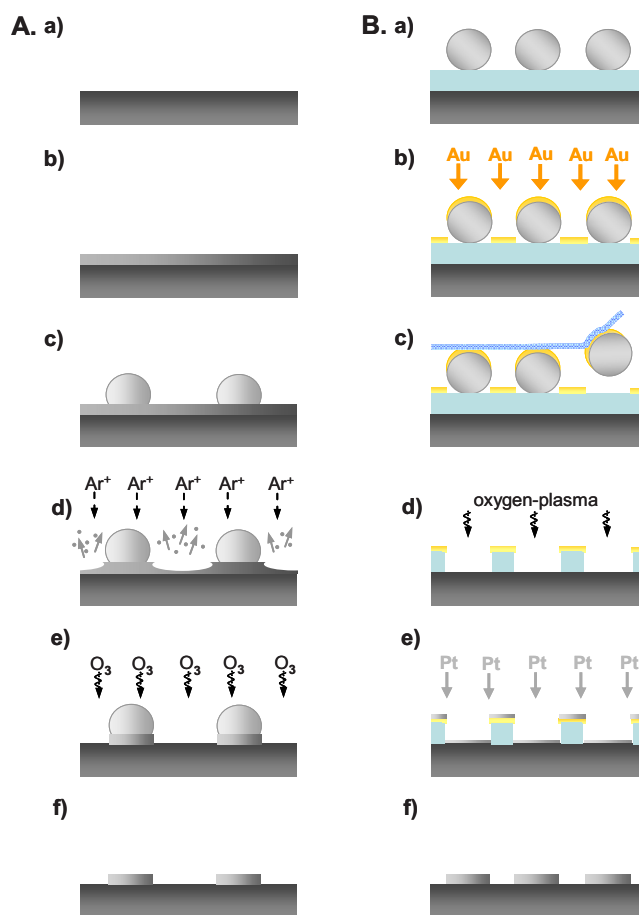


**Figure 1.** (Color online) Schematic presentation of the procedure for the preparation of the nanostructured Pt/GC electrodes: (A) CL starts with a polished GC substrate (a), followed by Pt film sputter deposition (b). On top of this, an adlayer of PS particles is deposited by dip coating which is relaxed into hemispherical shape (c). In the next step, the Pt film between the PS particles is removed by  $\text{Ar}^+$  sputtering (d), before finally the PS particles are removed by a  $\text{UV}/\text{O}_3$  treatment (e), leaving the Pt nanodisks (f). (B) HCL fabrication also starts with a polished GC substrate. Thereon, a sacrificial resist PMMA layer is deposited by spin-coating and masked with PS particles (a). In the next step, a Au layer is evaporated on top (b). The PS particles are removed by tape-stripping (c), resulting in the Au hole-mask. Afterward, the PMMA layer is removed underneath the unprotected holes in the Au mask by an oxygen plasma treatment (d), followed by Pt evaporation through the holes of the Au/PMMA mask (e). In the last step, the Au/PMMA mask is lifted-off in acetone (f).

V, 13.6 mA)<sup>26</sup> (compare Fig. 1A, d). To secure complete removal of the Pt film, not protected by the PS particles, we applied a slight overetching of  $\sim 30$  s, which results in Pt nanodisks supported on a GC neck.<sup>12</sup> Finally, the PS colloids were removed by reactive oxygen etching in a UV/ozone atmosphere for 75 min (Fig. 1A, e).

The nonstructured "Pt-free" sample (CL-00) was fabricated via the same sequence of substrate pretreatment, Pt deposition, and Ar<sup>+</sup> sputtering. In this case, the entire Pt film was removed (30 s overetch similar to the nanostructured sample preparation).

The nanostructured electrodes HCL-20 and HCL-10 were fabricated by hole-mask colloidal lithography, largely following the preparation procedure as specified by Fredriksson et al.<sup>13</sup> The GC substrates were first polished, chemically cleaned, and plasma treated by the same oxygen plasma procedure as described above. The Pt nanodisks were fabricated along the procedure schematically illustrated in Fig. 1B. A sacrificial resist poly(methyl methacrylate) (PMMA) layer and later, masking PS beads were deposited on the pretreated GC substrate (Fig. 1B, a). This was done by spin coating with PMMA and subsequent treatment in an oxygen plasma (5 s) to increase the hydrophilicity of the surface, followed by pipetting a thin polyelectrolyte layer on the PMMA surface, and finally the charged PS beads were deposited. Afterward, a plasma-resistant, 20 nm thick, Au film was evaporated on top (Fig. 1B, b) and the PS beads were removed by tape-stripping (Fig. 1B, c). This results in a masking Au film with well-defined holes (Au hole-mask) on the PMMA layer. During a subsequent oxygen plasma etching step, the Au covered area is protected, while the unprotected, bare PMMA film in the holes of the Au mask is removed (Fig. 1B, d). In the next step, Pt was deposited through the mask onto the GC surface (Fig. 1B, e). After removal of the hole-mask by a lift-off in acetone, the Pt nanodisks located in the former holes of the hole-mask remain on the surface, while the remaining part of the Pt film is removed together with the PMMA/Au film. This results in an array of Pt nanodisks with well-defined size and lateral distribution (Fig. 1B, f) similar to CL preparation, but without Ar<sup>+</sup> sputter removal of the Pt film characteristic of the latter approach.

The morphology of the nanostructured electrodes was examined by SEM using a LEO 1550 (Zeiss) instrument (10 kV operating energy, lateral resolution  $\sim 1.5$  nm). EDX analysis was employed for locally resolved elemental analysis of the nanostructured electrodes (EDX system Oxford Instruments GmbH, 6 kV operation energy). The EDX spectra were analyzed using the INCA 400 Oxford Instruments software.

Detailed structural information on the carbon-Pt interface was obtained from cross-sectional HRTEM images using a CM 20 microscope (Philips, 0.21 nm point-to-point resolution) operated at 200 kV and a Cs-corrected Titan 80–300 (FEI Company) operated at 300 kV. The cross-sectional samples were prepared by the standard preparation method, cutting small pieces of the nanostructured samples and gluing them together face to face. The resulting sandwich was sliced into thin vertical wafers, by mechanical grinding in a tripod, and subsequent ion milling, which thinned the received wedge down to electron transparency.

**Electrochemical and electrocatalytic characterization.**—The electrochemical and differential electrochemical mass spectroscopy (DEMS) measurements were performed in a dual thin-layer flow cell,<sup>27</sup> which allows for simultaneous electrochemical and mass spectrometric measurements under controlled continuous-flow conditions.<sup>28</sup> In brief, it consists of two coupled, differentially pumped vacuum chambers and a Balzer QMS 112 quadrupole mass spectrometer. The working electrode is pressed onto the first thin-layer compartment of the dual thin-layer flow cell (see Ref. 27 and 28). The second thin-layer compartment is connected to the mass spectrometer via a porous Teflon membrane, which assures that only volatile species can pass to the mass spectrometer. A delay of  $\sim 1$  s between faradaic and mass spectrometric current signal, due to the time required for the electrolyte to flow from the first to the second compartment, is corrected in the data presented. A constant flow of

the electrolyte was ensured by a syringe pump (World Precision Instruments, AL-1000) connected to the outlet of the dual thin-layer flow cell. The potential was controlled by a Princeton Applied Research model 263A potentiostat/galvanostat. A saturated calomel electrode served as reference electrode; all potentials, however, are quoted vs that of the reversible hydrogen electrode.

The supporting electrolyte (0.5 M sulfuric acid solution) was prepared using ultrapure sulfuric acid (Merck suprapur) and Millipore Milli-Q water. It was deaerated by high-purity argon gas (Westfalen Gase, N 6.0) before and during the electrochemical experiments. For CO electro-oxidation experiments, the base solution was saturated with CO (Messer-Griesheim, N 4.7).

Prior to the electrochemical measurements, the nanostructured Pt/GC electrodes were cleaned by rapid repetitive potential sweeps within a preset potential window (between 0.06 and 1.36 V) in order to remove organic contaminations, until a constant CV was obtained (100 mV s<sup>-1</sup>, typically 3–5 cycles).<sup>14,25,29</sup> For the CO<sub>ad</sub> stripping experiments, CO was adsorbed on the catalyst surface from a CO-saturated base solution at 0.06 mV for about 5 min. Subsequently, the cell was rinsed with CO-free base electrolyte ( $\sim 20$  min), and then the adsorbed CO was oxidized in an anodic potential scan up to 1.16 V (10 mV s<sup>-1</sup>). Following this scan, a base CV was recorded at a scan rate of 10 mV s<sup>-1</sup>. All experiments were performed at room temperature.

## Results and Discussion

**Surface characterization.**—Representative large-scale and high-resolution SEM images of the nanostructured Pt/GC electrodes with different geometric Pt coverage and of the reference sample (completely removed Pt film) are shown in Fig. 2. The large-scale images of the higher Pt coverage samples (Fig. 2a, c, g, and i) confirm the homogeneous distribution and narrow size distribution of the circular nanodisks expected from previous studies, both for the CL-prepared samples<sup>9–12</sup> (Fig. 2a and c) and for the HCL-fabricated samples<sup>13</sup> (Fig. 2g and i). For these samples, two-dimensional Fourier transforms yield distinct rings, reflecting the short-range order in the layer of nanodisks. In agreement with the real-space SEM images, there is no evidence for long-range order. The situation is different for the ultralow-loading sample (CL-01, Fig. 2e), where the nanodisks are irregularly distributed on the surface. Apparently, during CL fabrication the separation between the PS particles is so large that the electrostatic interactions between them are no longer strong enough to warrant a locally ordered distribution of them. Instead, it is dominated by the (random) spatial distribution of adsorbing PS particles. The images of the nonstructured Pt-free CL-00 sample (Fig. 2k and l) show a surface similar to the carbon surface between the Pt nanodisks of the CL-01 sample. The densities and sizes of the nanodisks evaluated from these images and the resulting Pt coverages are collected in Table I.

In the high-resolution SEM images, features between the Pt nanodisks are visible on the three nanostructured electrodes prepared via CL (Fig. 2b, d, and f). They are present also on the nonstructured sample (Fig. 2l), in a similar density. In contrast, no such features were observed in high-resolution images on the HCL-prepared samples (see Fig. 2h and j).

At this point, we tentatively associate these features with Pt nanoparticles which originate from Pt clusters formed during the Ar<sup>+</sup> sputtering process (see Fig. 1A, d), which is applied to remove the unprotected Pt film between the adsorbed PS colloids. This assignment agrees with their presence on the CL-prepared nanostructured electrodes, where the lithographic process includes an Ar<sup>+</sup> sputtering step for removal of Pt film, and their absence on the HCL-prepared samples, where Ar<sup>+</sup> sputtering is not employed.

In order to confirm the presence of Pt nanoparticles on the CL-prepared samples in between the Pt nanodisks, these areas were analyzed by EDX. In Fig. 3 we show representative overview EDX spectra recorded on a CL-40 (black, full line), CL-01 (blue, dashed line), CL-00 (olive, dotted line), and HCL-10 (lavender, dashed and dotted line) electrode in areas between the Pt nanodisks. Carbon and



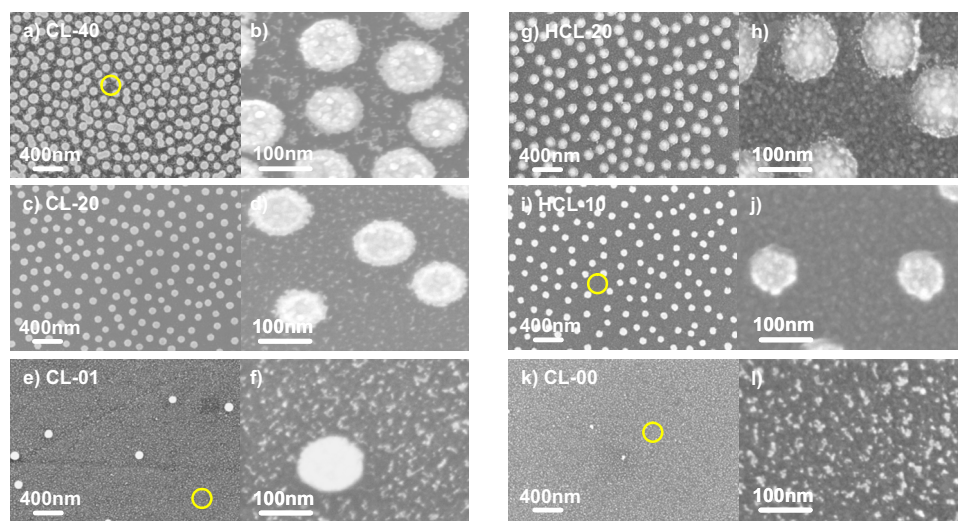


**Figure 2.** (Color online) Representative large-scale (a, c, e, g, i, k) and high-resolution (b, d, f, h, j, l) SEM images of the nanostructured Pt/GC electrodes. (a, b) High Pt coverage ( $\sim 43\%$ ) CL-prepared electrode (CL-40), (c, d) medium Pt coverage ( $\sim 26\%$ ) CL-prepared electrode (CL-20), (e, f) ultralow Pt coverage ( $\sim 7\%$ ) CL-prepared electrode (CL-01), (g, h) medium Pt coverage ( $\sim 22\%$ ) HCL-fabricated electrode (HCL-20), (i, j) low Pt coverage ( $\sim 10\%$ ) HCL-fabricated electrodes (HCL-10), and (k, l) a non-structured  $\text{Ar}^+$  sputtered electrode (CL-00) as reference. Large-scale images  $2.5 \times 3.4 \mu\text{m}$ ; high-resolution images  $330 \times 460 \text{ nm}$ . The bright circles in (a, e, i and k) denote the areas where the EDX analysis was performed.

oxygen are the predominant elements in the near-surface region (penetration depth of the primary electrons  $\sim 0.3 \mu\text{m}$ ), which is clearly demonstrated by the C  $K\alpha$  and O  $K\alpha$  peaks at 0.27 and 0.52 keV, respectively. In addition, Pt was also identified on the CL-40 sample in these areas (see, e.g., bright circle in Fig. 2a), despite the absence of Pt nanodisks, by the Pt M-peak at 2.05 keV (see also the inset in Fig. 3). Because of the close distance to the surrounding Pt nanodisks, however, this signal may well arise from scattered electrons which reached these nanodisks. Going to an ultralow-density CL-01 sample or to the CL-00 reference sample, the EDX-analyzed area (see bright circle in Fig. 2e and k, respectively) can be much further away from a Pt nanodisk. In these measurements, the Pt signal is considerably lower but still clearly detectable (0.08 and 0.06 atom %, respectively). In contrast to the CL-prepared samples, the amount of Pt detected between the Pt nanodisks on the HCL-10 electrode is at the detection limit of EDX analysis ( $<0.01$  atom %, see bright circle in Fig. 2i). The atomic ratios of the elements found in the EDX spectra, averaged over different areas between the Pt nanodisks, are given in Table II. An X-ray photoelectron spectroscopy analysis of the CL-00 sample,

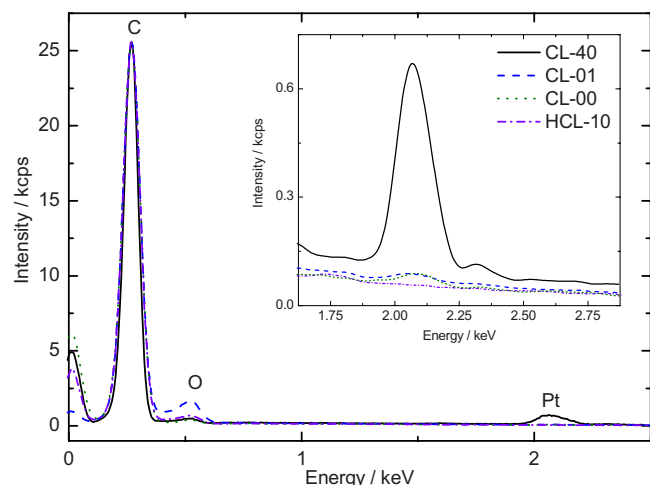


**Figure 3.** (Color online) EDX spectra of the CL- and HCL-prepared nanostructured Pt/GC electrodes showing overview spectra of CL-40 ( $\sim 43\%$  Pt coverage; solid, black), CL-01 ( $\sim 7\%$  Pt coverage; dashed, blue), nonstructured CL-00 (completely sputtered; dotted, olive) and HCL-10 ( $\sim 10\%$  Pt coverage; short-dashed, violet) electrode surfaces recorded in the areas marked in the SEM images in Fig. 2a, e, i, and k, respectively. The inset shows magnified details of the Pt region.

which is more surface sensitive than EDX, confirmed the EDX results and revealed a substantial amount of Pt on the surface of this sample.

Further information on the Pt nanoparticles is obtained from HRTEM images. The HRTEM image on the cross-sectional sample in Fig. 4a shows the trapezoidally shaped cross section of an individual Pt nanodisk. Furthermore, it reveals the presence of a thin layer of high-contrast nanoparticles close to or at the interface between GC and glue, in between the Pt nanodisks. The HRTEM images in Fig. 4b and c show details of the interface between Pt nanodisk and GC substrate. These images (Fig. 4b and c) further resolve that the features, which were already observed by SEM, are spherically shaped and  $\sim 5 \text{ nm}$  in diameter. Information on their structure can be derived from Fig. 4c, which resolves a face-centered cubic (fcc) structure of these spherical nanoparticles. This result further supports the EDX-based assignment of the features as Pt nanoparticles. They are also responsible for the numerous small white spots appearing on the GC substrate in the high-resolution SEM images (see Fig. 2b, d, f, and l). Similar type Pt nanoparticles were also seen on CL-prepared electrodes where the Pt layer was deposited by evaporation rather than by sputter deposition,<sup>25</sup> indicating that the nanoparticles are not formed during the deposition process, but rather during the final sputter-removal process. The nanoparticles spread over a layer of 5–10 nm thickness (Fig. 4a and b). The vertical distribution of the Pt nanoparticles may result both from the final sputter process (see above) and from the preparation of the TEM sample (“ $\text{Ar}^+$  thinning”).

A similar kind of HRTEM image of the cross section of a HCL-fabricated sample is shown in Fig. 4d. It displays a Pt nanodisk and a few surrounding nanoparticles, which are also located in the glue (Fig. 4e). The characteristic layer of nanoparticles observed on the CL-prepared samples is clearly absent on the HCL-fabricated sample. A few nanoparticles are still resolved both at the surface and

**Table II.** Atomic ratio of the elements determined from the EDX spectra (6 kV) in areas between the Pt nanodisks denoted by bright circles in Fig. 2a, e, i, and k on the CL-prepared model electrodes CL-40 and CL-01, the HCL-fabricated HCL-10, and on the nonstructured CL-00 sample, respectively.

Sample	C (atom %)	O (atom %)	Pt (atom %)
CL-40	97.5	1.4	1.1
CL-01	98.5	1.4	0.08
CL-00	98.2	1.7	0.06
HCL-10	97.0	3.0	0.01

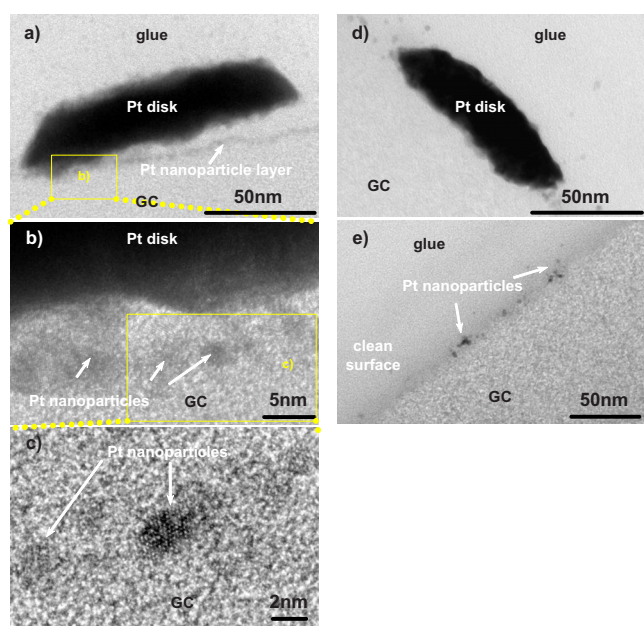


**Figure 4.** (Color online) TEM micrographs of the Pt/GC interface region. (a–c) Nanostructured Pt/GC electrodes prepared via CL (CL-20) and (d, e) via HCL (HCL-10). Scale bars and the assignment of the different areas are given in the images. Large-scale images (a, d)  $95 \times 140$  nm, (e)  $148 \times 225$  nm; high-resolution images (b)  $20 \times 30$  nm and (c)  $12 \times 18$  nm.

also distributed in the glue layer, where the latter seem to be related to the preparation of the TEM cross-section samples. Their density, however, is distinctly lower than on the CL-prepared nanostructured Pt/GC electrodes, where they form a homogeneous layer on the GC surface. This finding of essentially no Pt nanoparticles on the HCL-prepared nanostructured Pt/GC electrodes agrees also with the absence of Pt nanoparticles in the high-resolution SEM images of these samples (see Fig. 2j).

For determining the Pt coverage, i.e., the fraction of the GC area covered by Pt nanodisks and nanoparticles, we describe both of them by circular features. Considering only the Pt nanodisks, this results in Pt coverages of  $\sim 40\%$  (CL-40),  $\sim 22\%$  (CL-20 and HCL-20),  $\sim 10\%$  (HCL-10), and less than  $1\%$  (CL-01) for the different samples. Including also the Pt nanoparticles between the Pt nanodisks, the amount of the Pt-covered surface is slightly increased, by  $\sim 4\%$ , for the CL-40 and CL-20 electrodes. For the CL-01 samples, the difference is, on a relative scale, much bigger, leading to a Pt coverage of  $\sim 7\%$  (see Table I). The influence of the shape of the Pt nanodisks and nanoparticles on the accessible geometric Pt surface is discussed in the following section, together the roughness factor of these features.

In total, the electron microscopy analysis provided clear proof for the presence of small Pt nanoparticles on the CL-prepared nanostructured electrodes in the areas between the Pt nanodisks. These nanoparticles are about 5 nm in diameter and consist of high-contrast, fcc-structured material, which from the EDX results was identified as Pt. From the fact that they are present on the CL-prepared surfaces but negligible on the HCL-prepared electrodes, we conclude that their formation is related to the  $\text{Ar}^+$  sputtering step for Pt film removal, which is part of the CL processing but does not appear in HCL fabrication.

**Electrochemical characteristics.**—The electrochemical characteristics of the nanostructured Pt/GC electrodes were characterized by CV in base electrolyte and by the electrochemical (potentiodynamic) oxidation of a preadsorbed CO monolayer ( $\text{CO}_{\text{ad}}$  stripping). The latter was used also for determining the active surface area of the electrode, which gave results similar to the  $H_{\text{upd}}$  determined

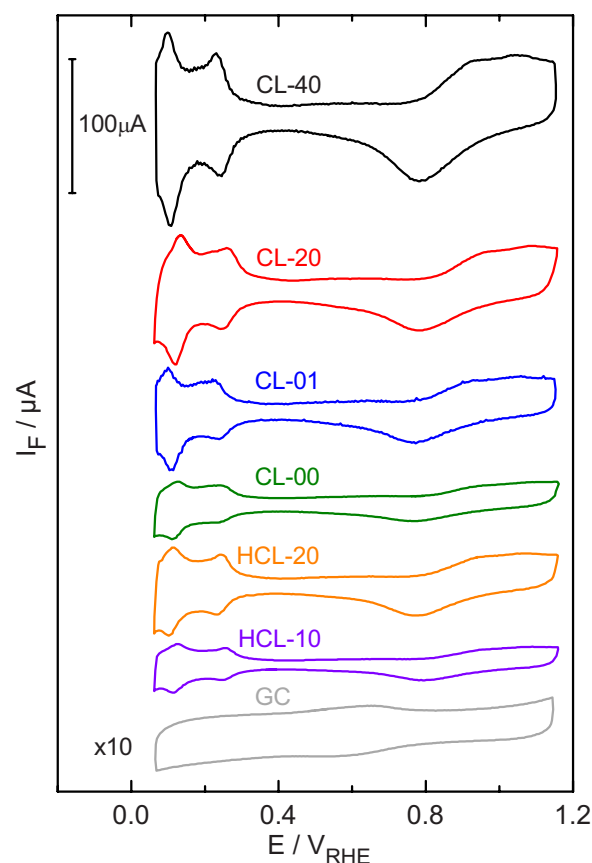


**Figure 5.** (Color online) Base voltammograms (scan rate  $100 \text{ mV s}^{-1}$ ) which were recorded on the different samples prepared via CL or HCL, respectively: CL-40 ( $\sim 43\%$  total Pt coverage, black), CL-20 ( $\sim 26\%$  total Pt coverage, red), CL-01 ( $\sim 7\%$  total Pt coverage, blue), nonstructured,  $\text{Ar}^+$  sputtered sample CL-00 (olive), HCL-20 ( $\sim 22\%$  Pt surface coverage, orange), and HCL-10 ( $\sim 10\%$  Pt coverage, lavender). A blank GC substrate (gray) is included as reference. Note that the signal for the GC sample is multiplied by a factor of 10.

surface areas, and area of the electrode, which gave results similar to the  $H_{\text{upd}}$  determined surface areas, and for calibrating the DEMS setup.<sup>27</sup> Electrocatalytic measurements on these and other nanostructured samples, focusing on the effects of density and size of the Pt nanodisks on the reaction mechanism, will be reported separately.<sup>23,24,30</sup>

**Electrochemical characterization.**—Figure 5 shows the resulting stable (see the Experimental section) faradaic signals recorded during cyclic base voltammograms at a sweep rate of  $100 \text{ mV s}^{-1}$  on the different electrodes. The characteristic  $H_{\text{upd}}$  features observed for the nanostructured CL- or HCL-prepared electrodes and that for the CL-00 sample clearly indicate that the surfaces contain different amounts of polycrystalline metallic Pt.<sup>31,32</sup> Due to contributions of the GC support, these samples generate higher pseudocapacitive features in the double-layer region compared to a polycrystalline Pt electrode.<sup>14,33,34</sup> For completeness, we also include a cyclic voltammogram recorded on a bare, unprocessed GC substrate (here the current signal is multiplied by a factor of 10). As expected, the characteristic  $H_{\text{upd}}$  features are missing on this sample, and the CV is dominated by oxidation and reduction peaks at about 0.6 V, which are generally attributed to the oxidative formation and reduction of quinones.<sup>35</sup> Comparing this CV with that recorded on the nonstructured CL-00 sample allows us to identify the contribution of the polished and acid/base-treated GC substrate to the CV of the latter sample. The total active Pt surface area on the CL- or HCL-prepared samples and on the nonstructured CL-00 samples was calculated by

**Table III.** Compilation of the active Pt surface areas determined by  $H_{\text{upd}}$ , the geometric Pt surface areas resulting from the SEM-based densities and sizes of the respective features (Pt nanodisks and Pt nanoparticles) and assuming different shapes of the Pt nanoparticles, and the resulting roughness factors of the different Pt/GC nanostructured electrodes. For the electrodes prepared by CL the Pt nanoparticles are included.

Sample	Pt~	Active Pt surface area (cm <sup>2</sup> )	Disk	Geometric Pt surface area (cm <sup>2</sup> )	
				Hemispheres	Spheres
CL-40	Nanodisks			0.178	
	Nanoparticles		0.008	0.017	0.034
	<b>Total</b>	<b>0.52</b>	<b>0.19</b>	<b>0.20</b>	<b>0.21</b>
	R-factor	2.9	2.8	2.7	2.4
CL-20	Nanodisks			0.099	
	Nanoparticles		0.011	0.023	0.045
	<b>Total</b>	<b>0.34</b>	<b>0.11</b>	<b>0.12</b>	<b>0.14</b>
	R-factor	3.4	3.1	2.8	2.4
CL-01	Nanodisks			0.003	
	Nanoparticles		0.017	0.034	0.068
	<b>Total</b>	<b>0.20</b>	<b>0.020</b>	<b>0.037</b>	<b>0.071</b>
	R-factor	56	9.6	5.2	2.7
CL-00	<b>Total</b>	<b>0.17</b>	0.020	0.04	0.079
	R-factor		8.5	4.3	2.1
HCL-20	<b>Total</b>	<b>0.23</b>		<b>0.104</b>	
	R-factor	2.2			
HCL-10	<b>Total</b>	<b>0.11</b>		<b>0.052</b>	
	R-factor	2.1			

assuming a  $H_{\text{upd}}$  monolayer charge on polycrystalline Pt of  $210 \mu\text{C cm}^{-2}$ <sup>36</sup> and a hydrogen coverage at the onset of bulk evolution of 0.77 monolayer. (For a detailed description of the integration procedure, including the determination of the onset potential, see Ref. 37.) Integrating the  $H_{\text{upd}}$  current in the cathodic-going scan and subtracting the double-layer contribution yields the active Pt surface areas given in Table III.

Relating the active Pt surface area to the exposed geometric Pt area of the electrode, the formal roughness factor (RF) for Pt was obtained. Gustavsson et al. reported an RF value of 2.6 for nanostructured electrodes prepared by CL.<sup>14</sup> (Note that in that study Pt was deposited by evaporation rather than by sputter deposition, as in the present study.<sup>25</sup>) In the present study similar values are obtained for the CL-40 and CL-20 samples (compare Table III, third column), considering only the Pt nanodisks on the electrode surface. Using the same approach for the CL-01 sample, however, results in an estimated roughness factor of 56. In a second calculation, we also considered the Pt nanoparticles on the electrode surface. Their geometrical shape was described by (i) circular flat disks, (ii) hemispheres, and (iii) spheres. For the calculations, we used the diameters and the densities derived from high-resolution SEM images (see Table I). The corresponding values for the geometric Pt surface area of the Pt nanoparticles are given in Table III. Relating the sum of the geometric Pt surface areas of the Pt nanodisks and the Pt nanoparticles to the electrochemically measured active Pt surface area leads to a decrease of the RF values of the CL-prepared electrodes. This decrease is a clear effect for the CL-40 and CL-20 samples and is dramatic for the CL-01 electrode. Assuming spherical Pt nanoparticles, the RF values of the CL-40 (2.4) and CL-20 (2.4) electrodes closely resemble those of the HCL-fabricated samples (2.2) and that of a pristine Pt film (2.5) electrode. For the CL-01 sample, the resulting RF value of 2.7 is still slightly higher than on the other nanostructured electrodes but in the same range of values. This is particularly true when considering that uncertainties in the approximation of the Pt nanoparticles size and shape will have the highest impact on this sample.

In total, the  $H_{\text{upd}}$  measurements fully support our previous conclusion of the presence of approximately spherical Pt nanoparticles on the GC surface in the areas between the Pt nanodisks of the CL-prepared nanostructured electrodes, while on the HCL-prepared electrodes they are essentially absent. In addition, they clearly demonstrate that the surface of these nanoparticles is electrochemically

accessible and that they are not covered by a carbon layer as expected, e.g., if they were embedded in the GC surface near region rather than being deposited on the GC surface.

**Preadsorbed CO monolayer oxidation.**—Representative  $\text{CO}_{\text{ad}}$  stripping traces are shown in Fig. 6. The  $m/z = 44$  mass spectrometric signals are normalized to the respective  $K^*$  value for direct comparison of the different samples. As shown in Fig. 6a, the characteristic  $H_{\text{upd}}$  features are suppressed on the  $\text{CO}_{\text{ad}}$ -blocked Pt surface of the Pt/GC electrodes. The characteristic feature of the CL-prepared nanostructured electrodes, the formation of a double peak for  $\text{CO}_{\text{ad}}$  stripping with two maxima at  $\sim 0.70$  and at  $\sim 0.75$  V, respectively,<sup>14,24</sup> is also observed in the present study on the high-loading (CL-40) and the medium-loading (CL-20) electrodes. In contrast, on the ultralow-loading CL-01 and the nonstructured sputtered CL-00 samples, we only find a single  $\text{CO}_{\text{ad}}$  stripping peak at the high-potential position ( $\sim 0.76$  V). The active Pt surface areas calculated from the  $\text{CO}_{\text{ad}}$  charge and assuming a  $\text{CO}_{\text{ad}}$  saturation coverage of 0.75 monolayer<sup>38</sup> are almost identical to those determined from the  $H_{\text{upd}}$  charge.

The time-delay-corrected  $m/z = 44$  ion current signals (see Fig. 6b) directly reflect the rate of  $\text{CO}_{\text{ad}}$  oxidation to  $\text{CO}_2$ . In the prewave region (0.4–0.6 V), the increasing mass spectrometric signal at  $m/z = 44$  (see  $\times 10$  magnified spectrometric traces) for CL-40, CL-20, HCL-20, and HCL-10 electrodes indicates the formation of small amounts of  $\text{CO}_2$  by  $\text{CO}_{\text{ad}}$  oxidation in this potential range.<sup>24,27</sup> In contrast, we find no such prewave signal on the CL-01 or on the CL-00 electrode. Similar findings (no measurable prewave  $\text{CO}_2$  formation) were reported also for a micelle-based Pt/GC nanostructured electrode,<sup>39</sup> indicating that the prewave is associated with results from  $\text{CO}_{\text{ad}}$  stripping from the polycrystalline Pt nanodisks. This agrees well with previous observations of prewave  $\text{CO}_{\text{ad}}$  oxidation on polycrystalline Pt.<sup>40,41</sup>

Double-peak features were repeatedly reported for  $\text{CO}_{\text{ad}}$  stripping, e.g., on sputter-cleaned polycrystalline Pt surfaces,<sup>42</sup> on preferentially oriented Pt nanoparticles,<sup>43,44</sup> or on single-crystal surfaces, including different facets of low-index planes.<sup>42,43,45</sup> They were generally attributed to the presence of differently oriented surface facets with differing  $\text{CO}_{\text{ad}}$  oxidation characteristics. For the present situation, this explanation appears unlikely. Instead, we favor an explanation which is based on reports of a shift of the  $\text{CO}_{\text{ad}}$



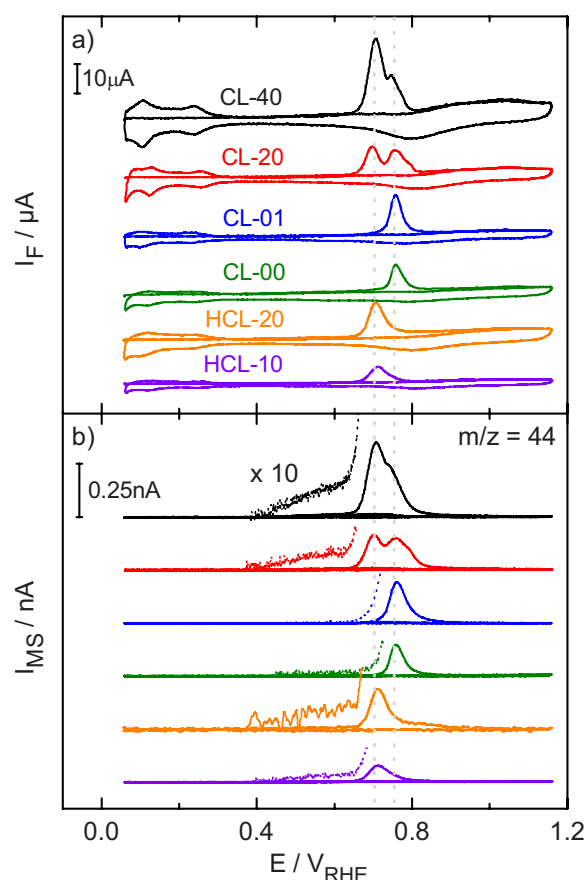


**Figure 6.** (Color online) Potentiodynamic  $\text{CO}_{\text{ad}}$  stripping and subsequent CV images in 0.5 M sulfuric acid (scan rate  $10 \text{ mV s}^{-1}$ , flow rate  $5 \text{ } \mu\text{L s}^{-1}$ ) recorded on nanostructured Pt/GC model electrodes prepared via CL or HCL: CL-40 ( $\sim 43\%$  total Pt coverage, black), CL-20 ( $\sim 26\%$  total Pt coverage, red), CL-01 ( $\sim 7\%$  total Pt coverage, blue), a nonstructured  $\text{Ar}^+$  sputtered CL-00 sample (olive), HCL-20 ( $\sim 22\%$  Pt coverage, orange), and HCL-10 ( $\sim 10\%$  Pt coverage, lavender). Prior to  $\text{CO}_{\text{ad}}$  monolayer oxidation, the model electrodes were saturated with CO at 0.06 V for 5 min and afterward rinsed with CO-free base solution for around 20 min. (a) Faradaic currents as measured and (b) mass spectrometric currents at  $m/z = 44$  normalized to the respective  $K^*$  values.

oxidation peak to higher potentials on smaller Pt nanoparticles<sup>27,35,46</sup> and of the formation of doublets due to agglomerate formation,<sup>35,46</sup> which the authors of the latter studies attributed to a particle size effect for  $\text{CO}_{\text{ad}}$  oxidation on Pt nanoparticles. Making use of this assignment, we propose that the low-potential  $\text{CO}_{\text{ad}}$  stripping peak is related to  $\text{CO}_{\text{ad}}$  oxidation on the polycrystalline Pt nanodisks, while the high-potential peak reflects  $\text{CO}_{\text{ad}}$  oxidation on the Pt nanoparticles. The contributions of the respective peaks to the total  $\text{CO}_{\text{ad}}$  stripping signal of the different CL-prepared nanostructured electrodes was determined by deconvolution of the mass spectrometric current signals of these samples, as illustrated in Fig. 7a-c. The resulting contributions from the two peaks are given in Table IV.

The numbers given in Table IV are mean values averaged over fits with slightly different parameters. For the CL-40 sample (Fig. 7a), the low-potential peak at 0.70 V contains  $\sim 70\%$  of the total  $\text{CO}_{\text{ad}}$  charge, indicating that the Pt surface of this nanostructured electrode is dominated by the Pt nanodisks. This result fits well to the determination of the respective geometric surface areas based on the SEM images, which yielded  $\sim 84\%$  on Pt nanodisks and about 16% on Pt nanoparticles. For the CL-20 structure (Fig. 7b), the corresponding values are  $55 \pm 5\%$  for the Pt nanodisks and  $45 \pm 5\%$  for the Pt nanoparticle surface. In this case, the possible error is larger because of the worse separation of the two  $\text{CO}_{\text{ad}}$

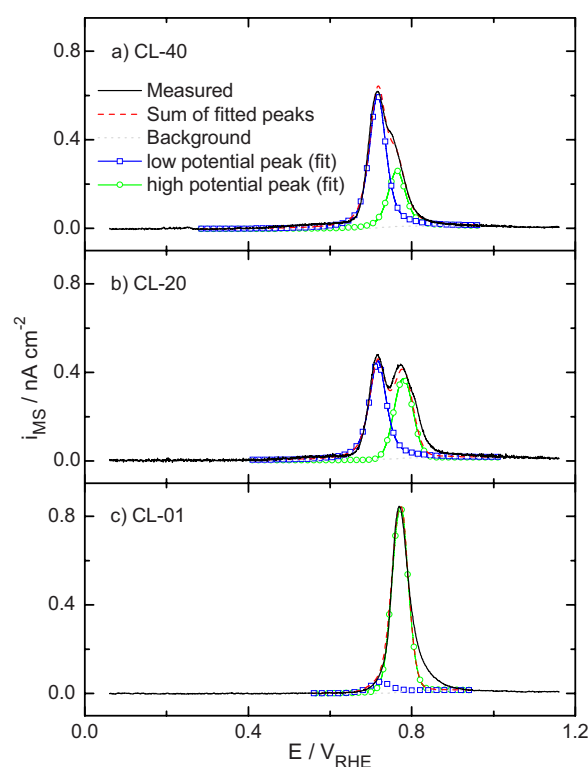


**Figure 7.** (Color online) Deconvolution of the  $m/z = 44$  mass spectrometric current signals recorded on CL-prepared, nanostructured Pt/GC electrodes during  $\text{CO}_{\text{ad}}$  monolayer oxidation into two peaks related to  $\text{CO}_{\text{ad}}$  oxidation on Pt nanostructures (low-potential peak, 0.70 V) and Pt nanoparticles (high-potential peak, 0.76 V): (a) CL-40, (b) CL-20, and (c) CL-01. The signals are normalized to the active Pt surface area of the respective electrodes for comparison. Solid, black – mass spectrometric current density; dotted, light gray – background; dashed, red – intensity of the fit of the two peaks; squares, blue – low potential peak (related to the Pt nanodisks), and circles, green – high potential peak (related to the Pt nanoparticles).

stripping peaks. For comparison, the SEM-based geometrical surface area evaluation resulted in a contribution of  $\sim 31\%$  of the surface area from the Pt nanoparticles, assuming spherical nanoparticles. The low-potential peak is narrow and high, whereas the high-potential peak is broader and lower. Finally, for the CL-01 sample,

**Table IV.** Peak positions and peak intensity ratios determined by deconvolution of the  $m/z = 44$  mass spectrometric current densities, and the geometric Pt surface areas related to Pt nanodisks and Pt nanoparticles on the different nanostructured Pt/GC electrodes described in Table I.

Sample	Peak position (V)	Pt structure	Fraction of the geometric Pt surface area (%)	Fraction of respective peak of the totals $\text{CO}_{\text{ad}}$ stripping signal (%)
CL-40	0.70	Nanodisks	84	$70 \pm 2$
	0.75	Nanoparticles	16	$30 \pm 2$
CL-20	0.70	Nanodisks	69	$55 \pm 5$
	0.76	Nanoparticles	31	$45 \pm 5$
CL-01	—	Nanodisks	5	$5 \pm 3$
	0.76	Nanoparticles	95	$95 \pm 3$
CL-00	0.76	Nanoparticles	100	—
HCL-20	0.71	Nanodisks	100	—
HCL-10	0.72	Nanodisks	100	—

there is only one dominant  $\text{CO}_{\text{ad}}$  oxidation peak at 0.75 V. The Pt nanodisks on this electrode are reflected by a small increase of the signal in the range from 0.66 to 0.72 V, which includes  $\sim 5\%$  of the total  $\text{CO}_{\text{ad}}$  charge, while the remaining 95% come from the Pt nanoparticles. Also, this result agrees well with the results from the SEM-based evaluation, where the Pt nanodisks contributed  $\sim 5\%$  to the total geometric Pt surface area. For the HCL-fabricated HCL-20 and HCL-10 samples, which only showed a single  $\text{CO}_{\text{ad}}$  stripping peak, the contribution of this peak was 100%.

In total, the clear correlation between the absence/presence of Pt nanoparticles on the nanostructured Pt/GC electrodes and the appearance of the high-potential  $\text{CO}_{\text{ad}}$  stripping peak, together with the qualitative agreement between the SEM-based Pt surface area and the charge in this peak, provide convincing proof that this peak arises from  $\text{CO}_{\text{ad}}$  oxidation on the Pt nanoparticles, in agreement with previous proposals of a particle-size-related upshift in  $\text{CO}_{\text{ad}}$  stripping peak.<sup>35,46,47</sup> Hence, this peak can be used for the unambiguous detection of Pt nanoparticles on these surfaces and for the quantitative evaluation of their surface area.  $\text{CO}_{\text{ad}}$  stripping demonstrated that nanostructuring via HCL does not cause Pt nanoparticle formation, whereas for CL fabrication Pt nanoparticles are abundant on the areas between the Pt nanodisks. On the ultralow-loading CL-prepared samples, the contribution from the Pt nanoparticles is dominant, but even on the medium-loading CL-prepared nanostructured electrodes it cannot be neglected.

### Conclusion

In order to clarify the discrepancy between the experimentally determined electrochemical properties of nanostructured Pt/GC electrodes with very low densities of Pt nanostructures ( $\varnothing 100\text{--}140\text{ nm}$ ) and those expected on the basis of their structural characterization, we have investigated these electrodes by electron microscopy, including high-resolution SEM imaging, HRTEM imaging, and locally resolved EDX analysis, and by electrochemical measurements, including base voltammetry and  $\text{CO}_{\text{ad}}$  stripping. The results clearly demonstrate that on nanostructured electrodes prepared by colloidal lithography, the areas between the Pt nanodisks are covered by a dilute layer of Pt nanoparticles of  $\sim 5\text{ nm}$  diameter. These were resolved in high-resolution SEM images and in HRTEM images, and were chemically identified by local EDX analysis. Using the particle sizes and densities determined by TEM and SEM, respectively, the contribution of the Pt nanoparticles to the geometric Pt surface area was calculated. It was found to result in a measurable increase of the Pt coverage on medium- and high-loading nanostructured electrodes, and in a dramatic increase on Pt/GC electrodes with very low densities of the Pt nanodisks, e.g., on a surface with 1% Pt coverage. Comparison with the active Pt surface areas determined by  $H_{\text{upd}}$  and the geometrical surface calculated for cylindrical Pt nanodisks and spherical Pt nanoparticles reveals a close correlation between these two parameters, which is reflected by an almost constant roughness factor of 2.2–2.8. In contrast, without considering the Pt nanoparticles, the roughness factors would vary between 2 and  $>50$ .

Furthermore, we found that the Pt nanoparticles can be identified electrochemically by their characteristic  $\text{CO}_{\text{ad}}$  stripping signal, which is upshifted from 0.70 to 0.76 V compared to  $\text{CO}_{\text{ad}}$  oxidation on the polycrystalline Pt nanodisks. The ratio between the charges in the two peaks agrees well with the trends expected from electron microscopy imaging, with a dominant high-potential peak for the ultralow loading CL-01 sample, comparable intensities for the higher Pt loading CL-prepared samples, and a dominant low-potential peak for the HCL-prepared samples. This assignment for the two  $\text{CO}_{\text{ad}}$  stripping peaks agrees well with previous proposals of a particle-size-induced upshift of the  $\text{CO}_{\text{ad}}$  stripping peak on Pt nanoparticles.

Finally, a developed lithographic technique, HCL, was introduced as an alternative method for preparing similar type nanostructured Pt/GC electrodes, and we could clearly demonstrate that the electrodes prepared via this method are essentially free from Pt

nanoparticles. HCL is proposed as the preferred method for the fabrication of nanostructured Pt/GC electrodes, and in particular, of electrodes with a low density of nanodisks.

### Acknowledgments

This work was supported by the Landesstiftung Baden-Württemberg via the Kompetenznetz Funktionelle Nanostrukturen (project B9), MISTRA (contract no. 95014), and the Swedish Energy Agency (grant no. P12554-1). We gratefully acknowledge A. Minkow (Institute of Micro- and Nanomaterials, Ulm University) for SEM and EDX imaging, and S. Tiedemann and A. Schneider (both from the Institute of Surface Chemistry and Catalysis, Ulm University) for developing a program for the evaluation of SEM images.

Ulm University assisted in meeting the publication costs of this article.

### References

1. D. R. Rainer, C. Xu, and D. W. Goodman, *J. Mol. Catal. A: Chem.*, **119**, 307 (1997).
2. R. M. Lambert and G. Pacchioni, *Chemisorption and Reactivity on Supported Clusters and Thin Films*, NATO ASI, Kluwer Academic Publishers, Dordrecht (1997).
3. C. R. Henry, *Surf. Sci. Rep.*, **31**, 231 (1998).
4. H. J. Freund, *Surf. Sci.*, **500**, 271 (2002).
5. P. W. Jacobs, F. H. Ribeiro, G. A. Somorjai, and S. J. Wind, *Catal. Lett.*, **37**, 131 (1996).
6. K. Wong, S. Johansson, and B. Kasemo, *Faraday Discuss.*, **105**, 237 (1996).
7. M. X. Yang, P. W. Jacobs, C. Yoon, L. Muray, E. Anderson, D. Attwood, and G. A. Somorjai, *Catal. Lett.*, **45**, 5 (1997).
8. F. Burmeister, C. Schäfle, T. Mattes, M. Böhmisch, J. Boneberg, and P. Leiderer, *Langmuir*, **13**, 2983 (1997).
9. C. Werdinius, L. Österlund, and B. Kasemo, *Langmuir*, **19**, 458 (2003).
10. P. Hanarp, D. Sutherland, J. Gold, and B. Kasemo, *Colloids Surf., A*, **214**, 23 (2003).
11. L. Österlund, S. Kielbassa, C. Werdinius, and B. Kasemo, *J. Catal.*, **215**, 94 (2003).
12. L. Österlund, A. Grant, and B. Kasemo, in *Nanocatalysis*, U. Heiz and U. Landman, Editors, Chap. 4, Springer Verlag, Berlin (2007).
13. H. Fredriksson, Y. Alaverdyan, A. Dmitriev, C. Langhammer, D. S. Sutherland, M. Zäch, and B. Kasemo, *Adv. Mater. (Weinheim, Ger.)*, **19**, 4297 (2007).
14. M. Gustavsson, H. Fredriksson, B. Kasemo, Z. Jusys, C. Jun, and R. J. Behm, *J. Electroanal. Chem.*, **568**, 371 (2004).
15. M. F. Crommie, C. P. Lutz, and D. M. Eigler, *Science*, **262**, 218 (1993).
16. R. D. Piner, J. Zhu, F. Xu, S. Hong, and M. V. Mirkin, *Science*, **283**, 661 (1999).
17. W. E. Morf, *Anal. Chim. Acta*, **330**, 139 (1996).
18. B. R. Scharifker, *J. Electroanal. Chem.*, **458**, 253 (1998).
19. W. E. Morf, *Anal. Chim. Acta*, **341**, 121 (1997).
20. W. E. Morf and N. F. de Rooij, *Sens. Actuators B*, **44**, 538 (1997).
21. W. E. Morf, M. Koudelka-Hep, and N. F. de Rooij, *J. Electroanal. Chem.*, **590**, 47 (2006).
22. E. J. F. Dickinson, I. Streeter, and R. G. Compton, *J. Phys. Chem. B*, **112**, 4059 (2008).
23. A. Schneider, L. Colmenares, Y. E. Seidel, Z. Jusys, B. Wickman, B. Kasemo, and R. J. Behm, *Phys. Chem. Chem. Phys.*, **10**, 1931 (2008).
24. R. Lindström, Y. E. Seidel, Z. Jusys, M. Gustavsson, B. Kasemo, and R. J. Behm, To be published.
25. Y. E. Seidel, R. Lindström, Z. Jusys, M. Gustavsson, P. Hanarp, B. Kasemo, A. Minkow, H. J. Fecht, and R. J. Behm, *J. Electrochem. Soc.*, **155**, K50 (2008).
26. D. Pettersson, M. Gustavsson, C. Lagergren, and G. Lindbergh, *Electrochim. Acta*, **51**, 6584 (2006).
27. Z. Jusys, J. Kaiser, and R. J. Behm, *Phys. Chem. Chem. Phys.*, **3**, 4650 (2001).
28. Z. Jusys, H. Massong, and H. Baltruschat, *J. Electrochem. Soc.*, **146**, 1093 (1999).
29. Z. Jusys and R. J. Behm, *J. Phys. Chem. B*, **105**, 10874 (2001).
30. Y. E. Seidel, A. Schneider, Z. Jusys, B. Wickman, B. Kasemo, and R. J. Behm, *Faraday Discuss.*, In press [DOI: 10.1039/b806437g].
31. H. Angerstein-Kozłowska, B. E. Conway, and W. B. A. Sharp, *J. Electroanal. Chem. Interfacial Electrochem.*, **43**, 9 (1973).
32. B. E. Conway, J. Barber, and S. Morin, *Electrochim. Acta*, **44**, 1109 (1998).
33. Y. Takasu, T. Fujiwara, Y. Murukami, K. Sasaki, M. Oguri, T. Asaki, and W. Sugimoto, *J. Electrochem. Soc.*, **147**, 4421 (2000).
34. O. V. Cherstiouk, P. A. Simonov, V. I. Zaikowskii, and E. R. Savinova, *J. Electroanal. Chem.*, **554–555**, 241 (2003).
35. F. Maillard, S. Schreier, M. Hanzlik, E. R. Savinova, S. Weinkauff, and U. Stimming, *Phys. Chem. Chem. Phys.*, **7**, 385 (2005).
36. V. S. Bagotzky, Y. B. Vassiliev, and O. A. Khazova, *J. Electroanal. Chem. Interfacial Electrochem.*, **81**, 229 (1977).
37. T. Biegler, D. A. J. Rand, and R. Woods, *J. Electroanal. Chem. Interfacial Electrochem.*, **29**, 269 (1971).
38. M. J. Weaver, S. C. Chang, L. W. H. Leung, X. Jiang, M. Rubel, M. Szklarczyk, D. Zurawski, and A. Wieckowski, *J. Electroanal. Chem.*, **327**, 247 (1992).
39. Y. E. Seidel, R. Lindström, Z. Jusys, J. Cai, U. Wiedwald, P. Ziemann, and R. J.



- Behm, *Langmuir*, **23**, 5795 (2007).
40. O. Wolter and J. Heitbaum, *Ber. Bunsenges. Phys. Chem.*, **88**, 6 (1984).
41. E. Santos, E. P. M. Leiva, W. Vielstich, and U. Linke, *J. Electroanal. Chem. Interfacial Electrochem.*, **227**, 199 (1987).
42. H. A. Gasteiger, N. M. Markovic, and P. N. Ross, *J. Phys. Chem.*, **99**, 16757 (1995).
43. J. Solla-Gullon, E. Herrero, F. J. Vidal-Iglesias, J. Feliu, and A. Aldaz, *Electrochem. Commun.*, **8**, 189 (2006).
44. V. P. Zhdanov and B. Kasemo, *Chem. Phys. Lett.*, **376**, 220 (2002).
45. A. M. De Becdelièvre, J. J. de Becdelièvre, and J. Clavilier, *J. Electroanal. Chem. Interfacial Electrochem.*, **294**, 97 (1990).
46. M. Arenz, K. J. Mayrhofer, V. Stamenkovic, B. B. Blizanac, T. Tomoyuki, P. N. Ross, and N. M. Markovic, *J. Am. Chem. Soc.*, **127**, 6819 (2005).
47. H. Ye, J. A. Crooks, and R. M. Crooks, *Langmuir*, **23**, 11901 (2007).